

Investigation of the Deposition of Microsphere Monolayers for Fabrication of Microlens Arrays

Pisist Kumnorkaew,[†] Yik-Khoon Ee,[‡] Nelson Tansu,[‡] and James F. Gilchrist^{*†}

Center for Advanced Materials and Nanotechnology, Department of Chemical Engineering, and Center for Optical Technologies, Department of Electrical and Computer Engineering, Lehigh University, Bethlehem, Pennsylvania 18015

Received April 8, 2008. Revised Manuscript Received April 29, 2008

Convective deposition of a monolayer of microspheres by drawing a meniscus of a suspension across a substrate is used to fabricate microlens arrays to enhance the photon extraction efficiency of light emitting diodes (LEDs). The self-assembly of a colloidal crystal within the blade-drawn thin film is dominated by capillary forces and the thickness of this crystal depends on many parameters, including the deposition rate and particle size. This study investigates these and other parameters such as angle and hydrophobicity of the deposition blade that have not previously been considered. Using a confocal laser scanning microscope, the local and long-range order of the deposited particles are evaluated by the radial distribution function, and the fraction of the number of nearest neighbors and local bond order, demonstrating the dependence of the microstructure on the deposition parameters. Our results suggest previous descriptions of the critical deposition parameters are inadequate for understanding how various processing conditions influence deposition. For instance, increasing the deposition blade angle from 20 degrees up to 90 degrees requires an increase in deposition rate to achieve a monolayer deposition. The microlens arrays were fabricated on LEDs where polystyrene and silica are coated in consecutive depositions. Heat is used to sacrifice the polystyrene layers to result in an ordered array of partially buried silica microspheres that act as lenses to scatter light from the device. Enhancement in light extraction efficiency of 2.66 times was demonstrated for InGaN-based light emitting diodes employing micron scale microlens arrays with 1 μm diameter silica microspheres.

Introduction

There is perhaps no simpler method of modifying surface properties than the deposition of particles of various compositions to alter a surface's roughness, reactivity, and optical properties. Controlled colloidal and/or nanoparticle deposition on substrates has an impact on fields such as catalysis,¹ photonics,^{2–4} lithography,^{3,5,6} ceramics,⁷ biocompatible surfaces,^{8,9} and sensors.^{9–11} Many applications are highly dependent on the microstructure (e.g., surface density, crystallinity, and orientation) of these modified surfaces. Many processes have been developed to facilitate particle deposition, such as spin coating,¹² epitaxy,^{13,14}

optical tweezers,¹⁵ electrophoretic assembly,¹⁶ and vertical deposition.^{17–19} Convective self-assembly offers the greatest promise in well-ordered, rapid, and controllable deposition on industrially relevant scales. The process outlined in this study utilizes a natural phenomenon coined the “coffee ring effect”²⁰ to draw particles to the edge of a droplet of suspension. The rate of drying dictates the mass transfer rate of particles toward the contact line, which is stationary or “pinned” as a result of the deposited colloids. Instead, by drawing the meniscus across a substrate this natural process has been utilized for controlled deposition, known as rapid convective deposition,²¹ a process seemingly similar to but distinctively different than the Langmuir–Blodgett technique for creating monolayer films.²² Although many recently developed processes take advantage of this technique, primary questions remain regarding the fundamental physics involved with particle convection and self-assembly.

The continuous convective assembly approach has been intensely considered because of its scalability. By vertically withdrawing a hydrophilized substrate from a low-volume-fraction particle suspension, colloidal particles crystallize on the substrate where a meniscus thin film is formed. Rapid convective deposition, shown in Figure 1, uses the horizontal deposition of a microliter droplet where a concentrated suspension is injected between the deposition blade and substrate. The small droplet of suspension is held by the capillary force between the blade

* Corresponding author. E-mail: gilchrist@lehigh.edu.

[†] Center for Advanced Materials and Nanotechnology.

[‡] Center for Optical Technologies.

(1) Tessier, P. M.; Velev, O. D.; Kalambur, A. T.; Rabolt, J. F.; Lenhoff, A. M.; Kaler, E. W. *J. Am. Chem. Soc.* **2000**, *122*, 9554–9555.

(2) Tessier, P. M.; Velev, O. D.; Kalambur, A. T.; Rabolt, J. F.; Lenhoff, A. M.; Kaler, E. W. *Adv. Mater.* **2001**, *13*, 396–400.

(3) Haes, A. J.; Haynes, C. L.; Richard, P.; Duyne, V. *Mater. Res. Soc.* **2001**, *636*.

(4) Im, S. H.; Lim, Y. T.; Suh, D. J.; Park, O. O. *Adv. Mater.* **2002**, *14*, 1367–1369.

(5) Haynes, C. L.; Van Duyne, R. P. *J. Phys. Chem. B* **2001**, *105*, 5599–5611.

(6) Zhang, Y.; Wang, X.; Wang, Y.; Liu, H.; Yang, J. *J. Alloys Compd.* **2008**, *452*, 473–477.

(7) Harris, D. J.; Hu, H.; Conrad, J. C.; Lewis, J. A. *Phys. Rev. Lett.* **2007**, *98*, 148301.

(8) Zhang, Y.; Wang, S.; Eghtedari, M.; Motamedi, M.; Kotov, N. A. *Adv. Funct. Mater.* **2005**, *15*, 725–731.

(9) Koyama, K.; Yamaguchi, N.; Miyasaka, T. *Science* **1994**, *265*, 762–765.

(10) Velev, O. D.; Kaler, E. W. *Langmuir* **1999**, *15*, 3693–3698.

(11) Yi, D.; Kim, M.; Turner, L.; Breuer, K.; Kim, D.-Y. *Biotechnol. Lett.* **2006**, *28*, 169–173.

(12) Jiang, P.; McFarland, M. J. *J. Am. Chem. Soc.* **2005**, *127*, 3710–3711.

(13) Blaaderen, A. V.; Hoogenboom, J. P.; Vossen, D. L. J.; Yethiraj, A.; Horst, A. V. D.; Visscher, K.; Dogterom, M. *Faraday Discuss.* **2003**, *123*, 107–119.

(14) Lee, W.; Chan, A.; Bevan, M. A.; Lewis, J. A.; Braun, P. V. *Langmuir* **2004**, *20*, 5262–5270.

(15) Biancianiello, P. L.; Crocker, J. C. *Rev. Sci. Instrum.* **2006**, *77*, 113702–10.

(16) Hayward, R. C.; Saville, D. A.; Aksay, I. A. *Nature* **2000**, *404*, 56–59.

(17) Dimitrov, A. S.; Nagayama, K. *Langmuir* **1996**, *12*, 1303–1311.

(18) Shimmin, R. G.; DiMauro, A. J.; Braun, P. V. *Langmuir* **2006**, *22*, 6507–6513.

(19) Diao, J. J.; Hutchison, J. B.; Luo, G.; Reeves, M. E. *J. Chem. Phys.* **2005**, *122*, 184710–5.

(20) Deegan, R. D.; Bakajin, O.; Dupont, T. F.; Huber, G.; Nagel, S. R.; Witten, T. A. *Nature* **1997**, *389*, 827–829.

(21) Prevo, B. G.; Velev, O. D. *Langmuir* **2004**, *20*, 2099–2107.

(22) Blodgett, K. B.; Langmuir, I. *Phys. Rev.* **1937**, *51*, 964.

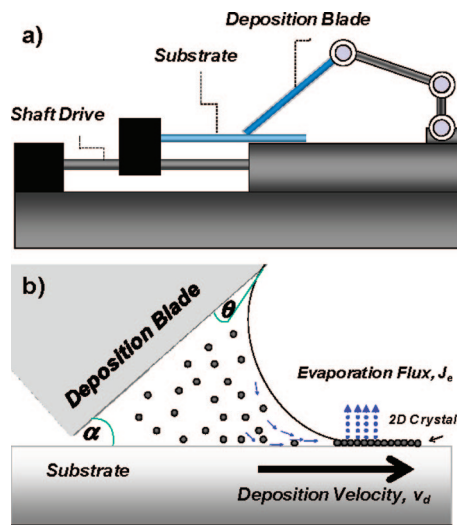


Figure 1. Experimental setup showing equipment (a) and the local deposition process (b) where a meniscus is pulled relative to the substrate to induce deposition and the local ordering of particles.

and substrate wedge, which in previous studies was fixed at an arbitrary angle of either 90° or less. The substrate is then translated by a linear motor as shown in Figure 1b. This technique also allows the use of a high volume fraction above 10% and a faster monolayer deposition speed (i.e., $20\text{--}90\ \mu\text{m/s}$ instead of $20\text{--}100\ \mu\text{m/min}$ via vertical deposition).

As the substrate is pulled away from the bulk suspension, the meniscus stretches out and sweeps across the substrate. The thickness of the meniscus gradually decreases from the bulk to the contact line where crystallization occurs. Particles from the bulk suspension move to the contact line by the liquid flow driven by evaporation^{20,23,24} and convective flow from the moving substrate. The particles most often self-assemble into a hexagonal close-packed structure at the "crystal front" as a result of the large capillary force²⁵ generated when the particles are in confinement in the thin film near where the three phases of the air/liquid/substrate meet. For monolayer crystal growth, the contact line is assumed to be the crystal front (i.e., the height of the meniscus at the crystal front must be equal to the particle diameter). If the height of the meniscus at the crystal front is less than the particle diameter, then the incoming particles will not form a close-packed structure. On the contrary, if the height of the crystal front is higher than the particle diameter, then multilayer crystals are formed.

Crystallization in this process was previously described by the equation proposed by Dimitrov and Nakayama²⁶ based on geometric considerations. The deposition rate v_d must be equal the crystal formation rate v_c , which depends on the particle volume fraction ϕ , evaporation flux J_e of the liquid medium, particle diameter d , and a deposition parameter, β as described by

$$v_c = v_d = \frac{\beta J_e \phi}{0.605d(1 - \phi)} \quad (1)$$

Here, β is a constant value²⁶ between 0 and 1 that depends on particle–particle and particle–substrate interactions. For low volume fraction and electrostatically stable particles, β approaches

1. The value decreases as particle–substrate interactions increase. Until now, β has not been systematically studied. It should also be noted that no other deposition parameters related to the fluid-flow properties are included in this model.

Two-dimensional (2D) colloidal crystals obtained from the convective deposition of submicrometer colloidal silica are used as an array of microlenses. Recently, microlens arrays have shown great potential in optical applications where the visible light is focused, collimated, or dispersed in a variety of applications including lighting, microscanning, and optical storage. Recently developed techniques for microlens array fabrication include beam-exposed methods such as UV proximity printing,²⁷ photoresist reflow,^{27,28} laser beam ablation,²⁹ and photolithography^{30,31} and polymeric microlenses via molding^{32,33} and hot embossing.^{34,35} Many of the methods for fabricating these microlens arrays are complicated or require specialized equipment, making scale up prohibitively expensive.

This study aims to investigate further the processing conditions surrounding rapid convective deposition and to demonstrate its use in the simple, scalable fabrication of microlens arrays for enhancing the light extraction efficiency of light-emitting diodes (LEDs). In this study, a substrate (either a glass substrate or the top GaN layer of the LED) is placed horizontally on a stage attached to the moving shaft drive as shown in Figure 1a. Monolayers of close-packed silica microspheres, which become the microlens arrays for an LED device, were deposited using convective deposition. The microlens arrays have been shown to enhance the light-extraction efficiency of an InGaN quantum well (QW) LED device.³⁶ The goal of this ongoing work is to understand better the fundamental physics and control morphology and microstructure of the deposited layers by probing previously unexplored parameters.

Materials and Methods

Suspension Preparation. The primary colloid suspension used in this work is prepared by dispersing silica microspheres (Fuso Chemical Co, Japan) having a density of $2.2\ \text{g/cm}^3$ and average diameters of 0.50 ± 0.01 and $1.01 \pm 0.02\ \mu\text{m}$ in deionized water with a volume fraction of $\phi = 0.2$. The suspension is dispersed using a sonic dismembrator (model 550, Fisher Scientific, Pittsburgh, PA) for 10 min and stirred for 30 min. (Fisher Scientific, model 550). For the fabrication of the microlens arrays, a separate solution of $1.1\ \mu\text{m}$ polystyrene (PS) prepared at $\phi = 0.2$ in DI water is used (supplied by the Emulsion Polymer Institute at Lehigh University). There is no added salt; therefore, the Debye screening length (κ^{-1}) is estimated to be 30 nm for each solution.

Substrate Preparation. Plain glass microslides ($76 \times 25 \times 1\ \text{mm}^3$, Fisher PA) are used as the deposition blade, and glass cover slides ($40 \times 24 \times 0.12\ \text{mm}^3$, Fisher PA) are used as the substrate for all samples prepared for analyzing the deposition process. All glassware is immersed in piranha solution (5:1 v/v sulfuric acid/hydrogen peroxide), used as a cleaning agent for 30 min. The

(27) Lin, C. P.; Yang, H.; Chao, C. K. *J. Micromech. Microeng.* **2003**, *748*.

(28) O'Neill, F. T.; Sheridan, J. T. *Optik* **2002**, *113*, 391–404.

(29) Naessens, K.; Van Daele, P.; Baets, R. Excimer Laser Ablation Based Microlens Fabrication in Polymer Materials; Lasers and Electro-Optics Society, 2002. LEOS 2002. The 15th Annual Meeting of the IEEE; Van Daele, P., Ed. 2002; pp 655–656, Vol. 2.

(30) Savander, P. *Opt. Lasers Eng.* **1994**, *20*, 97–107.

(31) Totsu, K.; Fujishiro, K.; Tanaka, S.; Esashi, M. *Sens. Actuators, A* **2006**, *130–131*, 387–392.

(32) Lee, B. K.; Kim, D. S.; Kwon, T. H. *Microsyst. Technol.* **2004**, *10*, 531–535.

(33) Shih, T.-K.; Chen, C.-F.; Ho, J.-R.; Chuang, F.-T. *Microelectron. Eng.* **2006**, *83*, 2499–2503.

(34) Chang, C. Y.; Yang, S. Y.; Huang, L. S.; Chang, J. H. *Infrared Phys. Technol.* **2006**, *48*, 163–173.

(35) Ong, N. S.; Koh, Y. H.; Fu, Y. Q. *Microelectron. Eng.* **2002**, *60*, 365–379.

(36) Ee, Y.-K.; Arif, R. A.; Tansu, N.; Kumnorkaew, P.; Gilchrist, J. F. *Appl. Phys. Lett.* **2007**, *91*, 221107.

(23) Wayner, P. C. *J. Colloid Interface Sci.* **1980**, *77*, 495–500.

(24) Stephan, K.; Zhong, L. C.; Stephan, P. *Heat Mass Trans.* **1995**, *30*, 467–472.

(25) Denkov, N.; Velev, O.; Kralchevski, P.; Ivanov, I.; Yoshimura, H.; Nagayama, K. *Langmuir* **1992**, *8*, 3183–3190.

(26) Dimitrov, A. S.; Nagayama, K. *Chem. Phys. Lett.* **1995**, *243*, 462–468.

glassware is then rinsed in DI water until no residual acid remains, and the clean glassware is immersed in DI water before use. The back and bottom edges of the glass deposition blade are either left hydrophilic or treated to be hydrophobic by adding a thin coating with parafilm (Fisher PA) in order to control the wetting region of the meniscus droplet. The contact angles on bare glass and on the hydrophobic surface are measured to be 10 and 105°, respectively, by imaging a 10 μ L stationary droplet on the surface. The InGaN/GaN quantum well LED devices were grown by metal–organic chemical vapor deposition (MOCVD), and the details of the growth and fabrication of the devices are available in previous studies.^{36,37} Prior to deposition, the GaN substrate is cleaned by soaking it in acetone and isopropanol alcohol (IPA) for 30 min each and then thoroughly rinsing in DI water until no residual IPA remains.

Deposition. The experimental setup is shown in Figure 1. This apparatus is contained within a humidity-controlled environment, where all experiments were performed at a constant 53% relative humidity and 24 °C, similar to typical laboratory conditions. The deposition blade angle is placed at a set angle of $25^\circ \leq \alpha \leq 80^\circ$ and approximately 10 μ m above the substrate, observed directly using a digital camera (Dinolite AM311S). Next 10 μ L of the colloid suspension is injected into the wedge between the substrate and deposition plate. The substrate is then pulled at a certain deposition speed ($20 \mu\text{m/s} \leq v_d \leq 90 \mu\text{m/s}$) using a linear motor (Harvard Instruments Co. Ltd.) as shown in Figure 1b.

Microstructure Analysis. Deposited monolayers are observed directly using SEM and confocal laser scanning microscopy (CLSM). A Hitachi 4300 field emission SEM is used to observe the microstructure. Confocal laser scanning microscopy (VTEye, Visitech International) is used to observe the microstructure of the thin film on the glass substrate over an area of $30 \mu\text{m} \times 30 \mu\text{m}$. For longer-range observations, the substrate is rewetted with an aqueous solution of 8 mM rhodamine B for imaging. A close investigation of the samples during rewetting shows that this method does not disturb the microstructure. The sample is scanned at 30 fps while sliding the sample across the microscope objective at 100 $\mu\text{m/s}$ using a motorized stage to image 3×10^5 particles over $30 \mu\text{m} \times 10 \text{mm}$. Likewise, multiple layers are imaged by scanning orthogonal to the substrate to obtain 3D particle locations.

Using algorithms developed by Crocker and Grier³⁸ and code developed by Professor Eric Weeks,³⁹ micrometer-scale particle locations are found with an accuracy of 40 nm in the x – y plane and 80 nm in the z direction. From these particle locations, the radial distribution function, $g(r)$, and coverage density, ρ , and distributions of the number of nearest neighbor, $\#NN$, and local bond order, ψ_6 , are used to describe the distribution and arrangement of the particles. $\#NN$ is calculated by counting the number of particles around a particle of interest within a distance of less than the second nearest neighbor distance of hexagonal close-packed crystals, $\sqrt{3}D$, where D is a particle diameter. $\#NN$ for hexagonal close-packed and square close-packed crystals equals 6 to 8, respectively. Moreover, $\#NN$ for a particle neighboring a point defect and next to a line defect equals 5 and 7, respectively. ψ_6 is a parameter that describes the orientation of a single particle in a crystal domain. It is calculated by using all angle θ information between particles of interest i and its nearest neighbors j with respect to a horizontal line. Prior to the computation, vectors r of i and j are determined for all nearest neighbors N as shown by

$$\psi_6(r_{ij}) = \frac{1}{N} \sum_{j=1}^N \exp[6i\theta(r_{ij})] \quad (2)$$

The radial distribution function is determined by using the mean number of particles n in a shell of width Δr at distance r , and the mean particle density ρ_p in each frame, $g(r) = n(r)/(\rho_p 4\pi^2 \Delta r)$. It has the highest value at the radial distance equal to the particle diameter

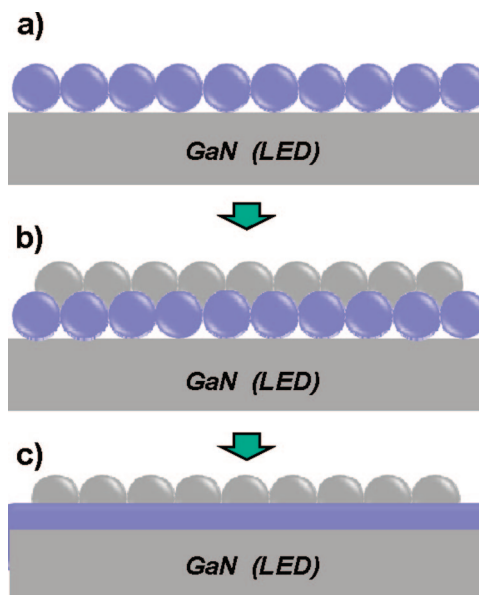


Figure 2. Deposition process to fabricate microlens arrays. (a) An initial monolayer of 1.1 μm polystyrene (PS) microspheres is deposited on the InGaN/GaN quantum well LED. (b) A second monolayer of 1.01 μm SiO₂ is deposited on top of the PS layer. (c) Heating above the melting temperature of PS partially submerges the SiO₂ microspheres, forming the desired geometry.

(i.e., $r/D = 1$, since the smallest distance between the two in a hard sphere particle is equal to the particle diameter). At $r \gg D$, $g(r)$ converges to the value of 1.

Microlens Array Fabrication. The microlens arrays fabricated on top of the GaN contact layer of the InGaN QW LEDs device structure similar to the configuration in refs 36 and 37 and these microlens arrays were fabricated by subsequent depositions of polystyrene and silica monolayers, as shown Figure 2. The layer of polystyrene was deposited, dried in air, and then rewetted with the silica suspension for deposition at 20 $\mu\text{m/s}$. Therefore, the polystyrene monolayer acts as the template for the deposition of the silica monolayer. The sample was heated above the melting temperature of the PS, $T_m \approx 240$ °C, such that the second layer of the silica monolayer was wetted by the melted polystyrene.

Result and Discussion

Meniscus Formation. This work demonstrates that the shape and curvature of the meniscus that resides between the deposition blade and the substrate has a surprisingly large effect on the resulting deposition. As shown in Figure 3, the blade angle and hydrophobicity of the deposition blade's rear face determines the quasi-static shape of the droplet. The blade is hydrophilic after the initial cleaning process described above, and when the suspension is introduced, it flows under the blade, wetting the underside of the blade along the full width of the substrate, as seen in the top row of images in Figure 3a. On this scale, surface tension dominates, and the resulting meniscus wets both surfaces equally to form a concave free surface. The degree of wetting on the back side of the blade increases with the deposition angle. At a deposition angle of 55°, the upper three-phase contact line pins at the upper corner of the blade. Above 55°, less suspension resides on the back side of the blade.

When the back side of the blade is treated to produce a hydrophobic surface, the suspension is pinned on the lower corner of the deposition blade, and no fluid flows to the back side at any deposition blade angle. In this case, a simple geometric argument describes the radius of curvature of the free surface at the front of the deposition blade,

(37) Arif, R. A.; Ee, Y.-K.; Tansu, N. *Appl. Phys. Lett.* **2007**, *91*, 091110–3.

(38) Crocker, J. C.; Grier, D. G. *J. Colloid Interface Sci.* **1996**, *179*, 298–310.

(39) Crocker, J. C.; Weeks, E. R. Particle tracking using IDL; <http://www.physics.emory.edu/~weeks/idl/>.

$$R = \left[\frac{W}{V} \left(\frac{\cos^2 \theta}{\tan(\alpha/2)} - \cos \theta \sin \theta - \frac{\pi}{2} + \theta + \frac{\alpha}{2} \right) \right]^{-0.5} \quad (3)$$

given by the deposition contact angle α , the liquid/substrate contact angle θ , volume of a droplet V , and the width of the substrate W . Figure 3b shows the agreement between measured and predicted radii, and a best fit gives $\theta = 25.6^\circ$. For different blade angles, the varying radius of curvature changes both the bulk pressure within the suspension and the profile of the extended meniscus near the substrate in the deposition region.

Deposited Morphologies. In this work, both the general morphology and the local microstructure of the deposited 2D crystals are characterized. Figure 4 shows the observed deposited morphologies that include submonolayer, monolayer, and multilayer colloidal arrays. The morphology primarily depends on the parameters of the deposition process and the suspension characteristics (i.e., the deposition rate, blade angle, blade hydrophobicity, solids volume fraction in suspension, relative humidity, and temperature). Within each of these morphologies, multiple microstructures are observed including randomly deposited colloids and both locally and long-range-ordered structures with various packings and symmetries. A monolayer is defined by the substrate that is fully covered by one layer of close-packed 2D crystal and is obtained by deposition at an optimal speed, v_{mono} . These monolayers are typically polycrystalline. Deposition speeds above v_{mono} result in partially coverage, so-called submonolayer, of particles. A multilayer thin film, in which more than one 2D crystal layer exists, is formed for deposition speeds lower than v_{mono} .

Although eq 1 gives a simple geometric description of the optimum deposition rate to obtain a given crystal thickness, it lacks an understanding of the effect of many processing parameters. For instance, changing the deposition angle or the hydrophobicity of the back side of the deposition blade has a large effect on v_{mono} .

Figure 5 is a set of phase diagrams identifying the morphology resulting from deposition at a given rate and blade angle. Experiments are conducted both for hydrophobic and hydrophilic deposition blades and the deposition of 0.5 and 1.0 μm particles. The black symbols (-•-) denote those experiments depositing a monolayer, thus at v_{mono} , whereas diamonds (\diamond) and open circles (\circ) represent the multilayer and submonolayer thin films, respectively.

In most cases, with increasing deposition angle, the deposition speed must increase in order to deposit a monolayer. Using the deposition blade having a hydrophobic backside, v_{mono} increases almost linearly in order to deposit a monolayer of both 0.5 and 1 μm SiO_2 microspheres, as shown in Figure 5a (top row). For the hydrophilic (bare glass) deposition blade, the optimum speed needed to form a monolayer is a weak function of deposition angle. The local minimum at $\alpha \approx 55^\circ$ is possible evidence of the pinning of the contact line at the corner on the back side of the deposition blade. For $\alpha < 55^\circ$, the three-phase contact line backside deposition corner is freely moving. In this regime, there is roughly a linear dependence between blade angle and v_{mono} .

The absolute magnitudes of v_{mono} are compared in Figure 5b. For 0.5 μm microspheres, the two curves cross over at $\alpha = 55^\circ$. Deposition using a hydrophilic blade requires faster deposition speeds to obtain a monolayer for $\alpha < 55^\circ$, whereas for $\alpha > 55^\circ$ the hydrophobic blade demonstrates higher values of v_{mono} . For 1 μm SiO_2 microspheres, v_{mono} is almost identical for $\alpha < 55^\circ$. For deposition angles $\alpha > 55^\circ$, v_{mono} diverges greatly. Whereas v_{mono} is consistently greater for smaller particles in each experiment, eq 1 is insufficient in describing the dependence of v_{mono} on deposition angle in the formation of monolayers; all

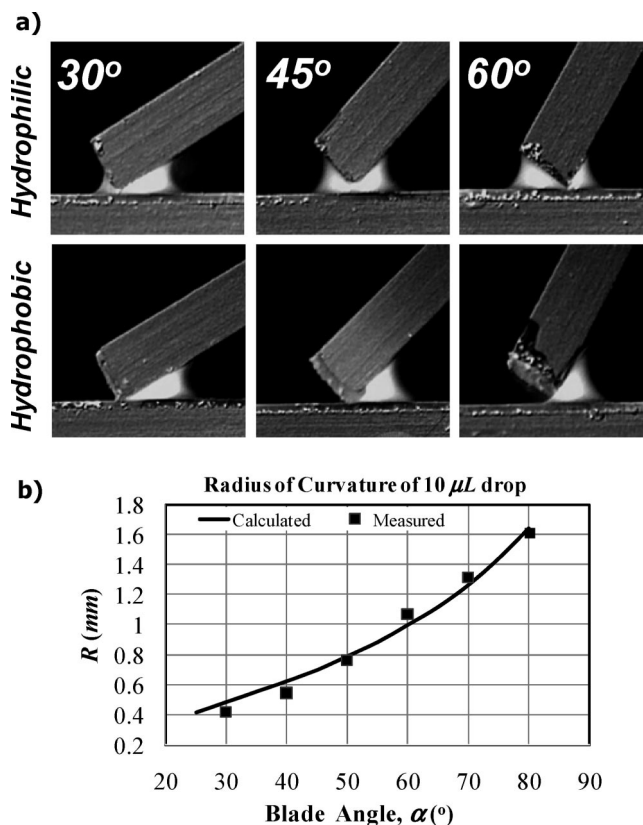


Figure 3. Radius of curvature shown as a function of contact angle. (a) Images of meniscus curvature (hydrophilic, top; hydrophobic, bottom). (b) Comparison between measured values and eq 3.

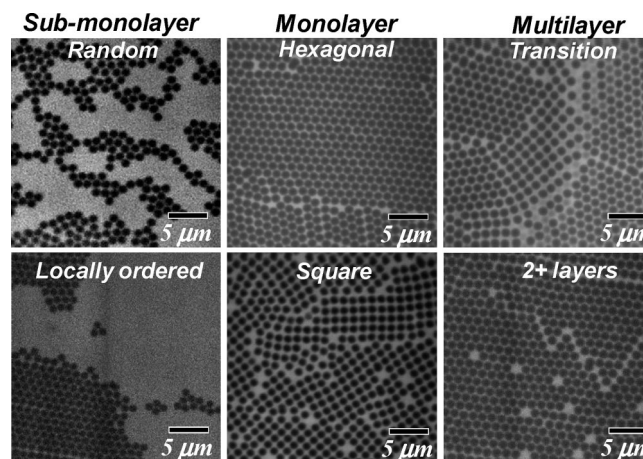


Figure 4. Three resulting morphologies are submonolayer, monolayer, and multilayer depositions. Various microstructures may exist, including random and locally ordered morphologies in the submonolayer regime, hexagonal and square close-packed monolayer crystals, and transition regions separating various microstructures formed in 3D.

profiles in these graphs would be flat. Previous work using dip coating to form monolayers, where essentially $\alpha = 90^\circ$, found an inverse relationship of v_{mono} on particle diameter. For the depositions using the hydrophilic blade, v_{mono} is roughly double for half the particle size; however, when a hydrophobic blade is used, large discrepancies with respect to this rule exist. This suggests that α alters other aspects of the deposition process, such as the evaporation rate.

Microstructure Analysis. Morphology alone does not give enough detail regarding the quality of a deposited monolayer, and processing conditions vary both the morphology and the

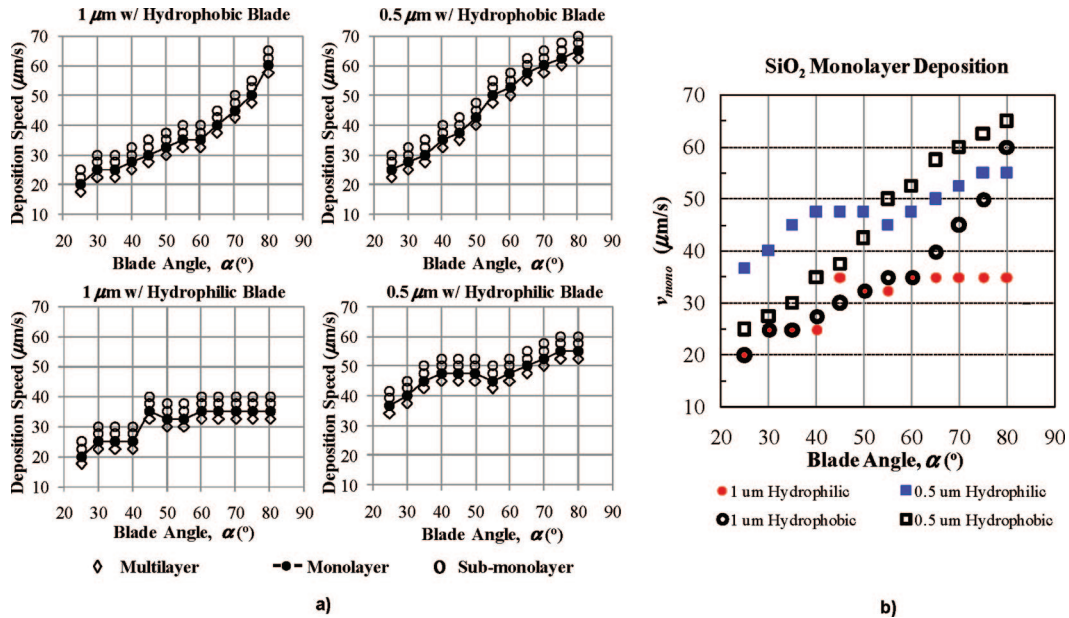


Figure 5. Deposition results. (a) Four phase diagrams describe the dependence of the morphology on deposition speed and blade angle, α . These experiments are repeated for two different particle sizes and by varying the hydrophobicity of the deposition blade. (b) Summarizing the results from these phase diagrams, clearly v_{mono} shows that a strong dependence on blade angle exists for hydrophobic blades whereas hydrophilic blades have a weaker dependence on blade angle. Previous predictions of deposition would suggest all of these profiles to be flat, independent of α .

microstructure. This is illustrated in Figure 6, where experiments were performed at $v_d = 60 \mu\text{m/s}$ at deposition angles of $\alpha = 35^\circ$, 55° , and 80° . All samples for which the microstructure is analyzed were deposited using a hydrophobic deposition blade. In this case, both $\alpha = 35^\circ$ and 55° result in the same surface coverage of $\rho = 0.4$, and $\alpha = 80^\circ$ has $\rho = 0.85$, which is close to the theoretical maximum of $\rho = \pi/(2\sqrt{3}) = 0.907$. Both experimental images obtained via confocal laser scanning microscopy and rendering images that highlight the local order parameter reveal the morphology and the microstructure in Figure 6a. In the rendered images, red spheres are those that have a number of nearest neighbors, $\#NN \neq 6$, blue spheres are those that are locally hexagonally close-packed (i.e., $\psi_6 > 0.9$), and green spheres have $\#NN = 6$ but $\psi_6 < 0.9$, indicating local disorder. Note that most green particles highlight line defects within the sample. The average ψ_6 for each image is indicated in Figure 6b. The morphology changes from submonolayer to monolayer, and the microstructure changes from random to locally ordered in the submonolayer regime and long-range order in the deposited monolayer at $\alpha = 80^\circ$.

The overall distribution of $\#NN$ for each image is shown in the top row of Figure 6b, distinguishing the locally disordered and the fully hexagonally close-packed structure. In the monolayer formed at $\alpha = 80^\circ$, most particles are hexagonally close-packed, represented by a single large peak at six $\#NN$, and the broader distribution is found for the random structure formed at $\alpha = 35^\circ$. At $\alpha = 55^\circ$, a single large peak also resides at $\#NN = 6$; however, particles located at the edge of each domain have $\#NN < 6$. Note that at both $\alpha = 35^\circ$ and 55° there are very few particles with $\#NN = 1$ and 0 because the capillary forces dominate local particle interactions during deposition. In randomly distributed microstructures, the local particle interactions do not have time to reach the optimal configuration before adsorbing to the substrate. Most deposition conditions still generate local order; however, if the electrostatic repulsion between the particles and the substrate was weaker, it would be more likely to produce disordered microstructures.

To characterize both local and long-range order, the radial distribution function, $g(r)$, is shown at the bottom of Figure 6b.

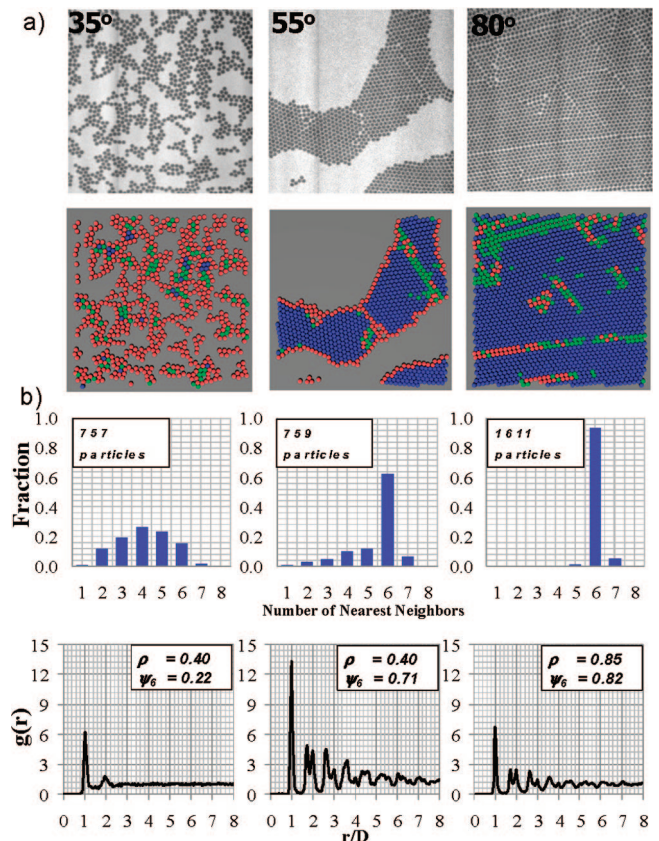


Figure 6. Microstructure analysis of thin films generated by varying the blade angle at a constant deposition speed of $60 \mu\text{m/s}$. (a) Images and particles identified for $\alpha = 35^\circ$, 55° , and 80° . (b) Number of nearest neighbor and radial distributions for each case. Whereas different deposition parameters can result in the same morphology, the microstructure depends on the blade angle. At v_{mono} (right), a highly ordered crystal is formed at higher blade angles.

In the random microstructure produced at $\alpha = 35^\circ$, only the first and second peaks, located at $r/D = 1$ and 2, are evident, consistent

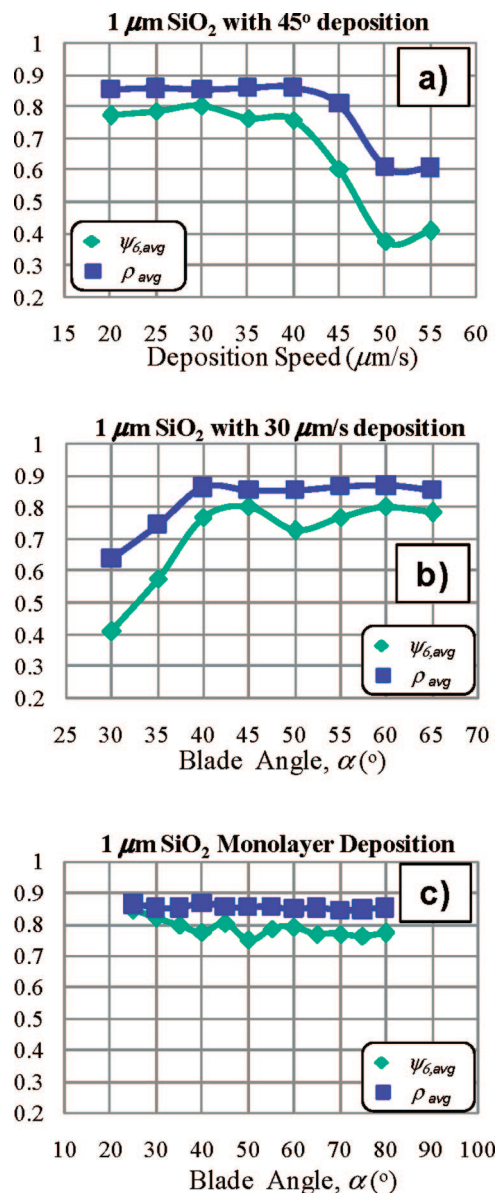


Figure 7. Measurements of $\psi_{6,avg}$ and ρ_{avg} averaged over $30 \mu\text{m} \times 10 \text{mm}$ samples. (a) Varying deposition speed at $\alpha = 45^\circ$ and (b) varying α for a fixed deposition speed of $30 \mu\text{m/s}$ show the transition between submonolayer and monolayer morphologies by indicating a change in density and crystallinity with increasing speed or decreasing angle, respectively. (c) The monolayer thin film deposited at v_{mono} for various α shows both roughly constant density and the crystallinity despite the processing conditions.

with the observation in rendered images and the $\#NN$ distribution. For both $\alpha = 55$ and 80° , this correlation function shows order as far as $r/D = 10$, with a second peak located at $r/D = \sqrt{3}$, reflecting the hexagonally close-packed orientation of these samples. The peaks are relatively higher in samples of lower density. These analyses were performed on a single image for each sample and could represent a bias due to local deviation in morphology. Therefore, the following represents data comprised over a scan area of 300 images representing single a continuous region that is $25 \mu\text{m} \times 10 \text{mm}$ in size.

Thin Film Quality. The average properties of local bond order $\psi_{6,avg}$ and average coverage density ρ_{avg} are used to qualify the thin film quality across a large range of the sample, as shown in Figure 7. These average properties are extracted from 300 frames scanned over 10 mm in length for each sample. The ρ_{avg} ranges from 0 (no particle) to a maximum of $\pi/(2\sqrt{3}) = 0.907$,

and $\psi_{6,avg}$ is in the range of 0 to 1, spanning no local hexagonal symmetry between particle neighbors to a long-range hexagonally close-packed crystal. For the fixed $\alpha = 45^\circ$, Figure 7a shows that ρ_{avg} slowly decreases with increasing deposition speed and drops significantly for speeds above $v_{mono} = 45 \mu\text{m/s}$. With regard to the local order, $\psi_{6,avg}$ is highest at a speed of $v_{mono} = 30 \mu\text{m/s}$, the optimal deposition speed for a thin film monolayer. Samples generated below v_{mono} show only a slight degree of disorder, but they are the analysis of the first layer of a multilayer deposition. Samples fabricated above $30 \mu\text{m/s}$ demonstrate a significant reduction in $\psi_{6,avg}$, although the density does not significantly decrease until the deposition rate is above $45 \mu\text{m/s}$. This indicates that the local order is highly sensitive to changes in the density and the number of defects grows substantially at deposition lower than v_{mono} . When the sample is clearly a submonolayer, above $45 \mu\text{m/s}$, the particles are distributed randomly, similar to the left image in Figure 6a.

For the fixed deposition rate of $30 \mu\text{m/s}$ at various deposition angles, $\alpha = 45^\circ$ is the condition for forming a monolayer at this speed. For $\alpha > 45^\circ$, ρ_{avg} is relatively constant in the first layer of deposition in the multilayer regime. The order parameter $\psi_{6,avg}$, is slightly lower than the maximum value found at $\alpha = 45^\circ$ as the result of an increased number of local defects in the crystal structure. Below $\alpha = 45^\circ$, $\psi_{6,avg}$ drops significantly, and ρ_{avg} is lower as a result of submonolayer deposition. Whereas the density between samples at $\alpha = 30$ and 35° decrease slightly, $\psi_{6,avg}$ differs significantly, suggesting that the microstructure changes from generally locally ordered to random as α decreases away from the ideal conditions for monolayer deposition. Finally, summarizing the properties of those experiments performed at v_{mono} for each blade angle in Figure 7c, no measurable differences are seen in the density or the structure of the monolayers.

Transition to Multilayer Microstructure. During some depositions at or near v_{mono} , localized perturbations in particle flux periodically form multilayer regions across the thin film. A transition region is always found between monolayer and multilayer regions in the form of loose square-packed microstructure. Cross-sectional imaging of multiple layers using z scans from the CLSM was used to investigate this transition phase in both the horizontal and vertical directions, as shown in Figure 8. Image analysis reveals that the microstructure changes from monolayer hexagonally close-packed to a loose square packing and then a square close-packed crystalline structure before the assembly of a hexagonally close-packed multilayer. The observation is similar to that of a 3D multilayer film using convective deposition conducted by Meng et al.,⁴⁰ where a geometric argument of the minimization of the surface energy describes the formation of these structures.

What is less clear is the defect densities found in consecutive layers formed via convective deposition. In previous studies of simple gravity-driven crystal assembly, defects are found more frequently near the substrate.⁴¹ A similar result is found for samples formed via rapid convective deposition shown in Figure 8b. This finding suggests that to reduce the number of defects in the crystals the consecutive deposition of monolayers will result in lower defect densities. This agrees with data presented in Figure 7a, where the monolayer formed at v_{mono} has a slightly higher $\psi_{6,avg}$ than the primary layers of the multilayer deposition. This monolayer acts as a template for subsequent layers. The rendered images also show that the primary axes of crystalline structures in the monolayer and multilayer regions are not related

(40) Meng, L.; Wei, H.; Nagel, A.; Wiley, B. J.; Scriven, L. E.; Norris, D. J. *Nano Lett.* **2006**, *6*, 2249–2253.

(41) Allard, M.; Sargent, E. H.; Lewis, J. A.; Kumacheva, E. *Adv. Mater.* **2004**, *16*, 1360–1364.

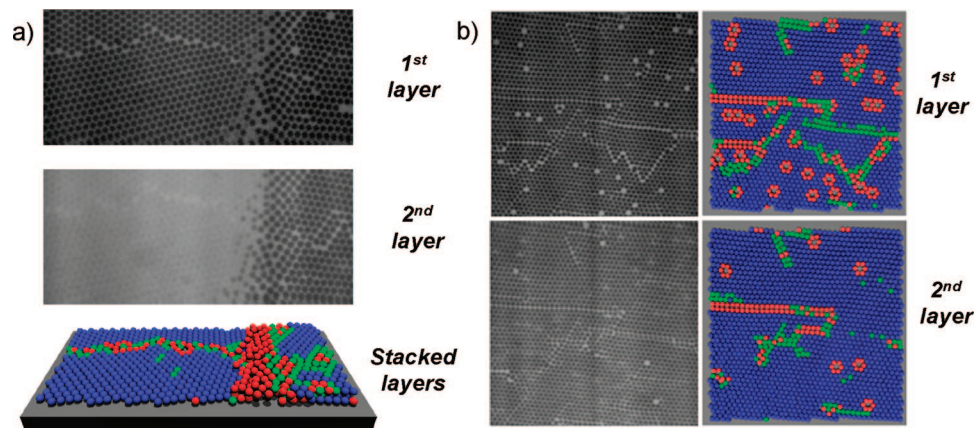


Figure 8. Three-dimensional vertical analysis of (a) the transition region where significant structural rearrangements occur and (b) the multilayer regime where more defects are found in the first layer than in higher layers. These images are of the same x - y region scanned in the z direction separated by 700 nm.

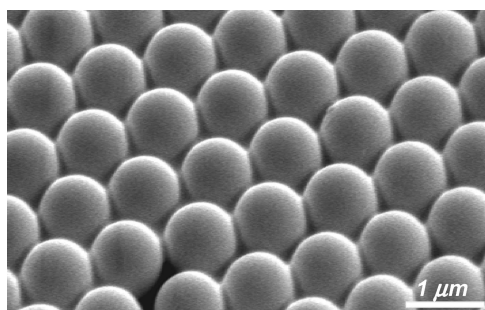


Figure 9. SEM of the microlens of 1 μm SiO_2 wetted by PS after subsequent depositions and heating. The hexagonally close-packed structure remains, and wetting occurs in well-ordered regions.

and the physics that dictate the orientation of crystals, grain boundaries, and line defects are not dictated by the parameters that are varied in this study.

Microlens Array Structure and Performance. Using the process outlined in Figure 2, subsequent depositions were used to form SiO_2 microspheres buried in PS to form microlens arrays on an MOCVD-grown InGaN/GaN QW LED substrate as shown in Figure 9. The LED studied here consists of four periods of InGaN QWs with 2.5 nm thickness and 12% In content, corresponding to a peak emission wavelength in the $\lambda_{\text{peak}} = 420$ nm regime. The details of the structure have been described.³⁶ The photoluminescence (PL) comparison studies were carried out on InGaN QW LED samples with and without microlens arrays to quantify the enhancement of light extraction efficiency with respect to the use of microlens arrays. The He-Cd laser excitation source operating at $\lambda = 325$ nm was used for the PL measurements, with the excitation source from the back side of the sample. The PL measurements were then collected from the top surface of the sample.

From our comparison studies shown in Figure 10, we found that the integrated PL intensities from the LED sample employing the microlens arrays show a 2.66-fold enhancement. This is in a good agreement with recent simulation studies performed on the structure.⁴² The peak luminescence is also enhanced 2.7-fold for the LED employing the microlens arrays. Recent experiments conducted on an electrically injected 480 nm emitting InGaN

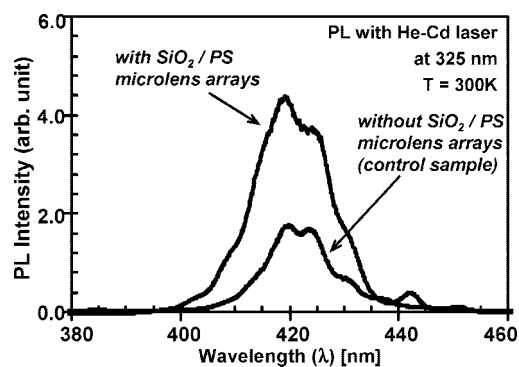


Figure 10. Room-temperature photoluminescence comparison measurements of a 2.5-nm-thick In_{0.12}Ga_{0.88}N QW sample ($\lambda \approx 420$ nm) with and without the SiO_2/PS microlens arrays.

QW LED with SiO_2/PS microlens arrays (with a diameter of 1 μm for SiO_2 microspheres) also result in a 219% improvement in the light output power.³⁶

Conclusions

The deposition of microsphere monolayers was demonstrated using controlled rapid deposition. It was seen that the hydrophobicity of the deposition blade and the blade angle have both a qualitative and quantitative effect on the optimum speed for monolayer deposition, ν_{mono} . By increasing the deposition contact angle, the particle flux to the meniscus increases by an unidentified mechanism related to the bulk pressure in the solution, resulting in increased deposition speeds to maintain thin film monolayers. It is assumed that the pressure gradient between the bulk suspension and atmosphere changes the fluid flow properties in a way that is uncaptured by previous models. The use of 2D and 3D confocal microscopy revealed the microstructure of particle arrangement in the thin film. Two main conclusions result from this analysis. First, changes in the blade angle, while shifting the actual value of ν_{mono} , have little influence on the microstructure for depositions at ν_{mono} but have a significant influence on the microstructure for depositions lower than ν_{mono} . Second, the existence of a transition phase between the monolayer and bilayer regions shows the instantaneous change in particle flux to the drying front. By observing grain boundary and crystal orientation, there is no relationship between the two regions next to the transition region. In the multilayer regions, the primary layer is found to be more disordered than the upper layers. Finally, the SiO_2/PS microlens arrays fabricated using this process have been

(42) Ee, Y.-K.; Kumnorkaew, P.; Tong, H.; Arif, R. A.; Gilchrist, J. F.; Tansu, N. *Comparison of Numerical Modeling and Experiments of InGaN Quantum Wells Light-Emitting Diodes with $\text{SiO}_2/\text{Polystyrene}$ Microlens Arrays*, Light-Emitting Diodes: Research, Manufacturing, and Applications XII, San Jose, CA, USA, 2008; SPIE: San Jose, CA, 2008; p 69100M-8.

demonstrated to enhance the light extraction efficiency in III-nitride LEDs, an approach that has strong potential for achieving a low-cost, practical solution in solid state lighting.

Acknowledgment. We thank the Emulsion Polymers Institute at Lehigh University for monosized PS samples. We also acknowledge the Royal Thai Scholarship for the support of P.K.

and the U.S. Department of Defense - Army Research Laboratory for the support of Y.-K.E.

Supporting Information Available: Movies of lateral and vertical scans of samples showing the techniques used for analysis. In addition, a derivation of eq 3 is given in detail. This material is available free of charge via the Internet at <http://pubs.acs.org>.

LA801100G